Energy Conversion and Management 353 (2026) 121205

Contents lists available at ScienceDirect

Energy Conversion and Management

journal homepage: www.elsevier.com/locate/enconman

Research paper

Dielectric characterisation of solar salt for volumetric heating applications in Power-to-Heat-to-Power systems

C. Valverde [a,*], G. Link [b], S. Soldatov [b], J.M. Catalá-Civera [c], P. Plaza-González [c], G. Dimitrakis [d], B. Singh [d], A. Cachot [e], L. Del Campo [e], M. Malki [e], M.M. Rodriguez-Garcia [a], E. Rojas [a]

[a] CIEMAT–Plataforma Solar de Almería, Ctra. de Senés, km. 4.5, Almería, 04200, Spain
[b] Karlsruhe Institute of Technology, Institute for Pulsed Power and Microwave Technology (IHM), Karlsruhe, 76344, Germany
[c] ITACA Institute, Universitat Politècnica de València, Camino de Vera, Valencia, 46022, Spain
[d] Department of Chemical and Environmental Engineering, University of Nottingham, Nottingham, NG7 2RD, UK
[e] CNRS, CEMHTI UPR 3079, Université d'Orléans, Orléans, 45071, France

ARTICLE INFO

Keywords:
Carnot battery (Power-to-Heat-to-Power)
Solar salt
Dielectric properties
Microwave-assisted heating
Cavity perturbation method
Electrochemical impedance spectroscopy

ABSTRACT

Carnot batteries, or Power-to-Heat-to-Power systems, rely on solar salt as a thermal energy storage medium and require efficient and controllable heating technologies. However, conventional resistive heating is constrained by the low thermal conductivity of solar salt, leading to temperature gradients, local overheating, and material degradation, which motivates the exploration of alternative volumetric heating approaches. In this context, this study evaluates the feasibility of microwave-based volumetric heating of solar salt by analysing its dielectric behaviour across both solid and molten states. Dielectric properties were measured using the cavity perturbation method at 912 MHz and 2.45 GHz with different sample volumes and electromagnetic field configurations. Under these conditions, the sharp increase in electrical conductivity in the molten state results in high effective dielectric losses that violate the small-perturbation assumption underlying this technique. Consequently, the microwave measurements were complemented by four-electrode electrochemical impedance spectroscopy from 100 Hz to 1 MHz up to 550 °C to confirm the dominance of ionic transport mechanisms. The results show activation energies of 0.810 eV in the solid state and 0.148 eV in the liquid state, while extrapolated conductivities of approximately 160–170 S m^{-1} correspond to microwave penetration depths of about 1.3 mm at 912 MHz and 0.8 mm at 2.45 GHz, providing an application-relevant measure of the interaction between molten solar salt and electromagnetic fields. These findings indicate that accurate dielectric characterisation of molten solar salt at microwave frequencies requires measurement systems specifically adapted to highly conductive liquids and suggest that effective microwave heating strategies may rely on solar salt-compatible ceramic materials combined with appropriately tailored electromagnetic field distributions.

1. Introduction

Electricity generation is a major contributor to greenhouse gas (GHG) emissions [1]. The thermal sector, comprising heating and cooling, accounts for half of global energy demand and is responsible for 40% of total CO_2 emissions [2]. Increasing the share of renewable energy sources (RES), such as solar photovoltaics and wind power, is essential to reduce fossil fuel-based electricity generation to 10% by 2050 [3].

However, the large-scale integration of variable RES introduces pronounced temporal mismatches between electricity generation and demand. A well-known manifestation of this challenge is the photovoltaic "duck curve", where high solar generation during midday leads to a deep reduction in net load, followed by steep ramping requirements in the evening as solar output declines. These rapid ramps are typically met by dispatchable, often fossil-based, generation assets [4]. As a result, decarbonisation of the electricity sector is only feasible with the integration of energy storage systems (ESS) capable of providing the required flexibility to mitigate RES intermittency. ESS can absorb surplus electricity during periods of overproduction and release it when demand exceeds supply, thereby smoothing net-load profiles and reducing reliance on conventional peaking plants [5]. Although demand-response strategies have been proposed to support grid balancing [6], they do not fully eliminate the need for ESS deployment, particularly under high RES penetration scenarios [7].

* Corresponding author.
E-mail address: cvalverde@psa.es (C. Valverde).

https://doi.org/10.1016/j.enconman.2026.121205
Received 7 December 2025; Received in revised form 5 February 2026; Accepted 6 February 2026
Available online 10 February 2026

Nomenclature

Parameters		**Acronyms**	
A	Pre-exponential factor, $S\,m^{-1}$	CB	Carnot Battery
c	Speed of light in vacuum, $m\,s^{-1}$	CPM	Cavity Perturbation Method
D_p	Penetration depth, m	CSP	Concentrated Solar Power
E_a	Activation energy, eV	EIS	Electrochemical Impedance Spectroscopy
E_{rms}	Root mean square electric field, $V\,m^{-1}$	EP	Electrode Polarisation
f_r	Resonant frequency, Hz	ESS	Energy Storage System
f_{geo}	Geometric cell factor, m^{-1}	HTF	Heat Transfer Fluid
H_{rms}	Root mean square magnetic field, $A\,m^{-1}$	IR	Infrared
j	Imaginary unit, $\sqrt{-1}$	ISM	Industrial, Scientific, and Medical (band)
k	Rate constant, s^{-1}	PID	Proportional–Integral–Derivative controller
k_B	Boltzmann constant, 8.617×10^{-5} eV K^{-1}	PtHtP	Power-to-Heat-to-Power
P	Absorbed electromagnetic power, W	QS	Quasi-static approximation
Q	Quality factor of resonant cavity	RES	Renewable Energy Sources
R	Electrical resistance, Ω	TES	Thermal Energy Storage
R_{dc}	Bulk (ohmic) resistance, Ω	UDR	Universal Dielectric Response
S_{21}	Forward transmission coefficient (S-parameter)	VNA	Vector Network Analyser
T	Temperature, K		
X	Reactance (capacitive or inductive), Ω		
Z^*	Complex impedance, Ω		
Z'	Real part of impedance (resistance), Ω		
Z''	Imaginary part of impedance (reactance), Ω		

Greek letters	
σ^*	Complex electrical conductivity, $S\,m^{-1}$
σ'	Real part of conductivity, $S\,m^{-1}$
σ''	Imaginary part of conductivity, $S\,m^{-1}$
σ_{dc}	DC conductivity, $S\,m^{-1}$
ε^*	Complex permittivity
ε'	Real part of permittivity (dielectric constant)
ε''	Imaginary part of permittivity (loss factor)
ε_0	Vacuum permittivity, $F\,m^{-1}$
$\tan\delta$	Dielectric loss tangent, $\varepsilon''/\varepsilon'$
μ^*	Complex magnetic permeability
μ'	Real part of magnetic permeability
μ''	Imaginary part of magnetic permeability (loss factor)
μ_0	Vacuum magnetic permeability, $H\,m^{-1}$
ω	Angular frequency, $rad\,s^{-1}$

Among existing storage technologies, battery energy storage systems (BESS) are widely used, particularly for small-scale applications. However, growing demand for long-duration and high-temperature storage has turned attention towards thermal energy storage (TES), which is better suited for storing excess renewable energy over extended periods [8]. The TES plays a key role in concentrated solar power (CSP) systems, with 45.5% of plants worldwide equipped with TES—amounting to 22 GW of capacity [9]. When combined with systems that convert electricity into heat and back into power, known as Carnot batteries (CB) or Power-to-Heat-to-Power (PtHtP), TES enables efficient reconversion of surplus renewable electricity into dispatchable energy.

The CBs make use of commercially available technologies [10], making them well-suited for large-scale deployment. A key advantage is their ability to repurpose decommissioned coal-fired power plants, offering a cost-effective pathway for energy infrastructure transition [11]. Their modular architecture – with separate storage tanks and power conversion units such as electric heaters or heat exchangers – enables flexible scaling, improved capacity factors, and reduced system costs. These benefits help mitigate the traditionally low round-trip efficiency associated with thermal-to-electric conversion systems [12].

Salt mixtures used as storage materials are solid at ambient conditions and melt at elevated temperatures. Their thermophysical properties make them suitable for use both as heat transfer fluids (HTFs) and TES media. Key advantages include high energy density, excellent thermal and chemical stability, low vapour pressure under operating conditions, broad availability at relatively low cost, and favourable safety characteristics such as non-flammability and non-toxicity [13].

The most commonly used salt mixture in TES systems for CSP plants is solar salt, a non-eutectic composition consisting of 60 wt% sodium nitrate ($NaNO_3$) and 40 wt% potassium nitrate (KNO_3), accounting for approximately 99.8% of the installed TES capacity worldwide [14]. It is operated in liquid form as a sensible heat storage medium over a temperature range typically bounded between 290 °C and 565 °C. The lower limit is set by the crystallisation temperature of the mixture (238 °C) with an operational safety margin, while the upper limit is dictated by the onset of thermochemical degradation [15]. At elevated temperatures, nitrate ions are partially reduced to nitrite ions through a reversible equilibrium, leading to progressive solar salt degradation. In conventional heating systems, the intrinsically low thermal conductivity of solar salt can promote localised overheating, accelerating nitrite accumulation and subsequent formation of oxide species and nitrogen oxides, which are known to contribute to corrosion processes [16]. To

date, CBs employing solar salt have primarily relied on surface-based heating approaches, such as electric resistance heaters, which further exacerbate thermal gradients within the storage medium [10]. These limitations have motivated the exploration of microwave-based heating as an alternative charging strategy, enabling volumetric heating and improved temperature homogeneity.

Microwave technology has broad potential across various sectors, driven by advances in material science and applicator design [17]. Microwaves are non-ionising electromagnetic waves in the 300 MHz to 300 GHz range that interact with materials at the molecular level by altering their electric (E) and magnetic (H) fields. This interaction produces heat through dielectric, magnetic, or conductive losses, depending on the material's properties [18].

Designing microwave processing systems requires knowledge of the temperature-dependent dielectric properties of the material [19]. Several measurement techniques are available, including the reflection, transmission–reflection, and resonance methods [20]. Among them, the cavity perturbation method (CPM), originally developed by Bethe and Schwinger [21], allows accurate determination of the complex permittivity (ε^*) by inserting a small sample into a resonant cavity and observing the shifts in resonant frequency ($\Delta f/f$) and quality factor (Q) [22]. Temperature-dependent measurements can be carried out either *in situ* – heating and measurement are performed simultaneously [23] – or by preheating the sample prior to its insertion into the cavity [24].

When the sample under test is a high-conductivity material, the assumption that the perturbed fields remain approximately the same as the original fields no longer holds. As a result, ε^* cannot be accurately calculated. In addition, the transmission coefficient (S_{21}) curve of the two-port network becomes shallower, making it difficult to determine the half-power bandwidth from the measured S_{21} data. An effective approach is to reduce the sample volume, thereby minimising E-field absorption by the high-loss material within the cavity [25]. To this end, Ma et al. [26] developed an improved CPM to measure ε^* of high-loss biological materials by adjusting the sample position, thus restoring the validity of the perturbation assumption and improving measurement accuracy. Moreover, Hachem et al. [27] demonstrated that the high ionic conductivity of molten salts can be exploited for dielectric characterisation by measuring temperature-dependent conductivity using a four-electrode electrochemical impedance spectroscopy (EIS) setup specifically designed for high-temperature liquid analysis. In their work, conductivity measurements were performed from 1 Hz to 1 MHz, between room temperature and 800 °C, for eutectic mixtures of molten salts used in thermal battery applications, such as the lithium fluoride–lithium chloride–lithium bromide eutectic (LiF–LiCl–LiBr).

With regard to the current state of the art in the dielectric characterisation of alkali nitrates and nitrites, Cornelison et al. [28] investigated the temperature-dependent centimetre-wave reflection of powdered sodium and potassium salts over the 2–20 GHz frequency range and temperatures from 25 °C to about 250 °C. Although the measurements were performed below the melting points of these materials, the study provides valuable insight into the dielectric response of alkali salts under electromagnetic fields. $NaNO_3$ exhibited negligible reflection losses, whereas KNO_3 showed significant losses as the temperature approached its order–disorder transition at 128 °C, attributed to the development of induced dipole moments as the lattice became increasingly disordered. However, the dielectric behaviour of solar salt itself, particularly across its phase transition has not been reported to date.

This work aims to assess the feasibility of using microwaves to achieve uniform heating of solar salt within a configuration suitable for large-scale CBs, motivated by the potential of microwave heating to enable volumetric energy deposition and mitigate the heat transfer limitations of conventional surface-based heating approaches. A prerequisite for such systems is reliable knowledge of the temperature-dependent complex permittivity of solar salt under operating conditions. Given the difficulty of obtaining accurate ε^* for materials exhibiting high ionic conductivity, the analysis combines results from three different setups employing the CPM for high-temperature dielectric characterisation. The three cavities operate with different sample volumes: in one, heating and measurement are performed simultaneously, whereas in the other two, the sample is first heated in a conventional furnace, held at the target temperature for a sufficient period, and subsequently transferred to the cavity, where $\Delta f/f$ and Q-factor variations are recorded. Most measurements were performed at 2.45 GHz, with complementary tests at 912 MHz. Additional experiments at the H-field antinode showed measurable magnetic interaction, although significantly weaker than the response under predominant E-field excitation, indicating that microwave heating in solar salt is governed primarily by conduction losses.

To complement the high-frequency data, electrical conductivity (σ) measurements were also performed using four-electrode EIS over the 100 Hz–1 MHz frequency range and at temperatures up to 550 °C. These results provide insight into the behaviour of solar salt at lower frequencies, confirming the sharp increase in ionic mobility during melting and the predominance of frequency-dependent dielectric losses associated with ionic currents in the liquid state. Taken together, the combined CPM and EIS results provide a systematic assessment of the interaction of solar salt with electromagnetic fields across relevant frequency ranges and temperatures. To the authors' knowledge, this represents the first study to explicitly address both the response and practical measurement limitations of solar salt under microwave excitation, thereby establishing a quantitative basis for the design of microwave-based heating concepts for PtHtP applications.

The remainder of this paper is structured as follows. Section 2 describes the experimental methods, including the fundamentals of microwave heating, the CPM employed for high-temperature dielectric characterisation using different resonant cavities, and complementary EIS measurements. Section 3 presents and discusses dielectric properties from CPM and conductivity from EIS, while Section 4 summarises the main conclusions and outlines perspectives for future work.

2. Materials and methods

2.1. Fundamentals of microwave heating

Electromagnetic waves in the microwave range interact with matter in the form of reflection, transmission, and absorption, depending on the material's electromagnetic properties. Only the absorbed fraction of energy contributes to heating, as the E- and H-fields induce energy dissipation within the material, leading to dielectric, magnetic, and conductive (Joule) losses. The relative contribution of each mechanism depends on the intrinsic properties of the material, such as its electric permittivity, magnetic permeability, and electrical conductivity [29].

The material's response to the E-field is characterised by its dielectric constant (ε'), which quantifies energy storage through charge polarisation, and its loss factor (ε''), which represents the ability to dissipate energy as heat. Both parameters are components of ε^*, defined in Eq. (1), which governs the conversion of microwave energy into thermal energy in non-magnetic materials, and depend on variables such as frequency, temperature, material composition, and particle size [30].

$$\varepsilon^* = \varepsilon' - j\varepsilon'' \tag{1}$$

The polarisation of dipoles or electric charges under an alternating E-field results in dielectric loss [31]. In materials with high σ, conduction loss dominates the heating process due to the generation of eddy currents in the alternating E-field. The E-field drives free charges through the material, resulting in resistive heating [32]. The total (effective) loss component of ε^* can be expressed as the sum of dielectric and conductive contributions:

$$\varepsilon''_{\text{eff}} = \varepsilon''_{\text{diel}} + \frac{\sigma'}{\omega\varepsilon_0} \tag{2}$$

where $\varepsilon''_{\text{diel}}$ represents the intrinsic dielectric losses of the material, σ' is the real part of electrical conductivity, ω is the angular frequency, and ε_0 is the vacuum permittivity.

In the case of purely conductive losses ($\varepsilon''_{\text{diel}} \approx 0$), this reduces to:

$$\varepsilon''_{\text{eff}} = \frac{\sigma'}{\omega\varepsilon_0} \tag{3}$$

From ε^*, the penetration depth (D_p) can be obtained. This is defined as the distance from the surface of the sample at which the E-field amplitude decreases by a factor of $1/e$, where e denotes Euler's number:

$$D_p = \frac{c}{\omega}\sqrt{\frac{2\left[1+\sqrt{1+(\tan\delta)^2}\right]}{\varepsilon'(\tan\delta)^2}} \tag{4}$$

where δ is the dielectric loss angle, representing the phase lag between the E-field and the material polarisation response, and $\tan\delta = \varepsilon''_{\text{eff}}/\varepsilon'$ is the loss tangent, $\varepsilon''_{\text{eff}}$ being the total (effective) loss factor including both dielectric and conductive contributions, and c is the speed of light in vacuum.

Similar to dielectrics, an external alternating H-field interacts with magnetic materials. This interaction is described by the complex magnetic permeability (μ^*), defined in Eq. (5), which is composed of a real part, or permeability (μ'), and an imaginary part, or magnetic loss factor (μ'') [33]:

$$\mu^* = \mu' - j\mu'' \tag{5}$$

Magnetic losses can arise from hysteresis, eddy currents, domain wall motion, and electron spin resonance in the presence of an alternating H-field. An alternating H-field causes magnetic dipoles in magnetic materials to oscillate. Because magnetic domains tend to remain aligned in a fixed direction, the field must reverse to demagnetise and reorient them, producing a hysteresis loop. The energy dissipated is proportional to the area of this loop [34].

In conductive materials, the varying H-field also induces an electromotive force (Faraday's law), which drives currents that cause resistive heating [35].

The electromagnetic power (P) absorbed by a material depends on the penetration of microwave radiation into the material and is given by:

$$P = 2\pi f\varepsilon_0\varepsilon''_{\text{eff}}E^2_{\text{rms}} + 2\pi f\mu_0\mu'' H^2_{\text{rms}} \tag{6}$$

where μ_0 is the vacuum magnetic permeability, and E_{rms} and H_{rms} are the root mean square values of the E- and H-fields, respectively.

2.2. Cavity perturbation method

The most widely used methods for the dielectric characterisation of materials are the transmission line method, the free-space method, and the CPM. However, in the case of solar salt – whose operating temperature range in the liquid state lies between 290 °C and 565 °C – the CPM is particularly well suited for temperature-dependent measurements, as it allows stable sample containment, accurate temperature control, and *in situ* — dielectric characterisation under high-temperature liquid conditions [36]. The main limitation of this method is the small sample size it requires. Molten salt mixtures, with high ionic mobility, exhibit high values of ε'', as given by Eq. (2). This, in turn, results in a high $\tan\delta$ and a reduced D_p. Authors such as Dakermandji [37] classify materials with $\tan\delta$ greater than 0.1 at industrial, scientific, and medical (ISM) frequencies as 'very high-loss' materials. Accurate analysis of the interaction with the electromagnetic field requires mitigating the effects of the large dielectric losses. In practice, this is achieved through the use of thin samples or dedicated cavity adaptations.

2.2.1. Dual mode cylindrical cavity for dynamic measurement of dielectric properties

A dual-mode cavity was employed to simultaneously heat and measure ε^* of cylindrical samples (10 mm diameter, 15 mm height). A cross-coupling filter ensured high isolation between the heating mode (transverse electric, TE_{111}) and the measuring mode (transverse magnetic, TM_{010}), as shown in Fig. 1. The heating signal was generated by one vector network analyser (VNA) and amplified by a narrowband solid-state amplifier (2.2–2.6 GHz, ~50 dB gain, 150 W maximum output), while the measuring signal was provided by a second VNA. Heating rate was controlled via a proportional–integral–derivative controller (PID) by adjusting the input frequency sweep and coupling level. Sample temperature was monitored using an infrared (IR) pyrometer through a dedicated aperture, which inferred the temperature of the sample from the measured temperature of the quartz tube wall. A separate aperture allowed insertion of the quartz tube. All apertures were designed to minimise microwave leakage and maintain the integrity of the cavity field distribution.

An enhanced CPM, combined with a quasi-static (QS) approximation [38] and a new formulation, is used to determine ε^* while eliminating cavity wall losses, as described in detail in [19]. Under the QS assumption, samples contained in holders are analysed using three configurations: the empty cavity (unperturbed), the cavity with the empty holder, and the cavity with the sample-filled holder.

Within this framework, ε' and ε'' are related to the normalised $\Delta f/f$ and the change in inverse Q ($\Delta(1/2Q)$) as follows:

$$\varepsilon' = 1 + \frac{-\frac{\Delta f}{f}\left(\eta + N\frac{\Delta f}{f}\right) - N\left[\Delta\left(\frac{1}{2Q}\right)\right]^2}{\left(\eta + N\frac{\Delta f}{f}\right)^2 + N^2\left[\Delta\left(\frac{1}{2Q}\right)\right]^2} \tag{7}$$

$$\varepsilon'' = \frac{\eta\,\Delta\left(\frac{1}{2Q}\right)}{\left(\eta + N\frac{\Delta f}{f}\right)^2 + N^2\left[\Delta\left(\frac{1}{2Q}\right)\right]^2} \tag{8}$$

Here, N is the depolarisation factor along the E-field direction (determined through calibration using reference materials with known ε^*), and η is the sample filling factor, defined as:

$$\eta = \frac{\int_{V_s}|E_0|^2\,dv}{2\int_{V_c}|E_0|^2\,dv} \tag{9}$$

where E_0 denotes the E-field distribution of the empty-cavity resonant mode, V_s is the sample volume, and V_c is the cavity volume.

The normalised $\Delta f/f$ and the change in inverse Q are expressed as:

$$\frac{\Delta f}{f} = \frac{f_2 - f_1}{f_1} \tag{10}$$

$$\Delta\left(\frac{1}{2Q}\right) = \frac{f_1}{f_2}\frac{1}{2}\left(\frac{1}{Q_2} - \frac{1}{Q_1}\right) \tag{11}$$

where f_1 and Q_1 are the unloaded resonant frequency and quality factor of the cavity with the empty sample holder, and f_2 and Q_2 correspond to the cavity with the sample-filled holder.

For low-loss materials, sample insertion may lead to an increase in the measured Q, resulting in non-physical negative values due to the contribution of cavity wall losses. To remove this effect, $\Delta(1/2Q)$ is corrected by accounting for the variation in stored electric energy induced by the dielectric sample. Using the measured $\Delta f/f$, the corrected expression is given by:

$$\Delta\left(\frac{1}{2Q}\right) = \frac{f_1}{f_2}\frac{1}{2}\left(\frac{1}{Q_2} - \frac{1}{Q_1} - \frac{1}{Q_0}\frac{f_2^2 - f_1^2}{f_0^2}\right) \tag{12}$$

where f_0 and Q_0 refer to the empty, unperturbed cavity (without the sample holder).

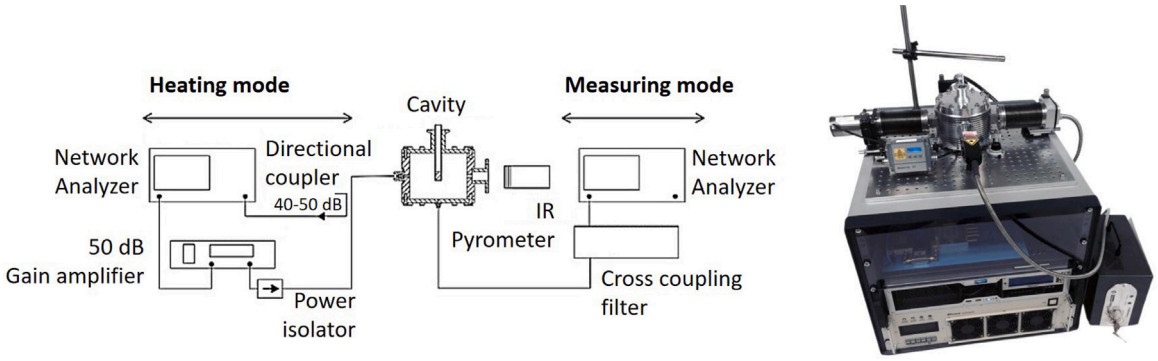

Fig. 1. Scheme of the testing device for dielectric properties using a cylindrical cavity and dual mode (left), and the manufactured dual-mode microwave cavity (right) [19].

2.2.2. Rectangular cavity for high-temperature dielectric measurements

This design (Fig. 2) consists of a rectangular cavity operating in the TE_{104} mode, based on a WR340 waveguide incorporating a 10-mm-wide iris at both ends, followed by waveguide-to-coax transitions. The signal is generated by a VNA connected to the resonator through two coaxial-waveguide adapters. Unlike the previously described system, this setup requires preheating the sample in a resistive tubular furnace. The sample, contained in a quartz tube with an internal diameter of 8 mm, is introduced into the cavity through a guiding mechanism. To avoid convective cooling during transfer, an insulating block is placed between the furnace and the cavity. The cavity includes two opposite apertures located in the regions of maximum E-field: one for inserting the quartz tube and another for an IR pyrometer, which provides a direct measurement of the sample's surface temperature during operation. Two additional apertures are also present in the regions of maximum H-field.

Dielectric properties are retrieved using a synthetic calibration approach based on full-wave electromagnetic modelling of the complete cavity-sample system [24]. The forward problem is solved by reproducing the experimental geometry in CST Microwave Studio, a commercial full-wave electromagnetic solver, and computing the two-port scattering parameter matrix $\mathbf{S}(f)$ of the resonator for prescribed values of ε' and ε''. The transmission coefficient $S_{21}(f)$ is used to characterise the resonance behaviour, from which f and Q are extracted.

In the CPM framework, ε' and ε'' can be expressed as:

$$\varepsilon' = 1 + \frac{V_c}{AV_s}\frac{f_1 - f_2}{f_2} \tag{13}$$

$$\varepsilon'' = \frac{V_c}{BV_s}\left(\frac{1}{Q_1} - \frac{1}{Q_2}\right) \tag{14}$$

where A and B are calibration coefficients accounting for field redistribution effects inside the sample. By sweeping ε' and ε'' within physically admissible bounds and computing the corresponding S_{21} responses, the inverse problem is solved by minimising the mismatch between simulated and experimental resonance parameters. Once the optimal $(\varepsilon', \varepsilon'')$ pair is identified, the corresponding simulated (f_1, Q_1, f_2, Q_2) values are used to determine the coefficients A and B.

2.2.3. Cylindrical cavity for high-temperature dielectric measurements at 912 MHz and 2.45 GHz

The experimental setup consists of a single cylindrical cavity operating in different TM_{0n0} modes: TM_{020} at 912 MHz and TM_{050} at 2.45 GHz. A quartz tube with an internal diameter of 4 mm is inserted into each cavity. A VNA records f and Q after an initial measurement of the empty tube. The system also includes a computer running a customised control programme and a motorised platform that transfers the sample between the cavity and an electrically controlled furnace (Fig. 3). Experiments are conducted at 912 MHz and 2.45 GHz, both located within the ISM frequency band. After being maintained at the target temperature for 10 min to ensure thermal homogeneity, the sample is lowered into the cavity. ε^* is then determined from the $\Delta f/f$ and the change in Q between the loaded and empty cavity [39].

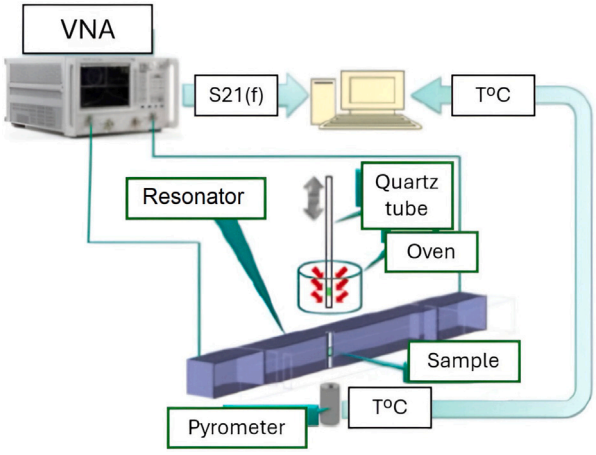

Fig. 2. Schematic of the setup for measuring microwave properties in a rectangular TE_{104} cavity [24].

2.3. Electrochemical impedance spectroscopy

The complex electrical conductivity (σ^*) of solar salt was determined using a four-electrode configuration specifically designed for high-conductive liquids. This arrangement provides higher accuracy than the conventional two-electrode method by minimising polarisation effects at low frequencies and high temperatures and by reducing impedance contributions from the wiring [40]

The experimental system (Fig. 4) consists of a measuring probe made up of two platinum (Pt) wires positioned between two Pt plates, which are immersed in the liquid sample contained in a crucible. The current is applied between the outer plates, while the potential is measured at the inner Pt tips. The entire assembly is housed in an alumina sheath inserted into a closed vertical tubular furnace capable of reaching up to 1600 °C under air or gas flow [41]. A mobile micrometric system allows the electrodes to be immersed approximately 8 mm into the molten salt, while the temperature is monitored by an S-type thermocouple positioned close to the surface of the melt. A gold–palladium (Au–Pd) crucible containing 48.3 g of solar salt (29.0037 g $NaNO_3$ + 19.3377 g KNO_3) was used, with an inner diameter of 40 mm and an effective sample height of 21 mm.

The salt was preheated to 550 °C before starting the measurements. From this temperature, three thermal cycles were performed: (i) cooling to room temperature, (ii) heating to 550 °C followed by cooling, and

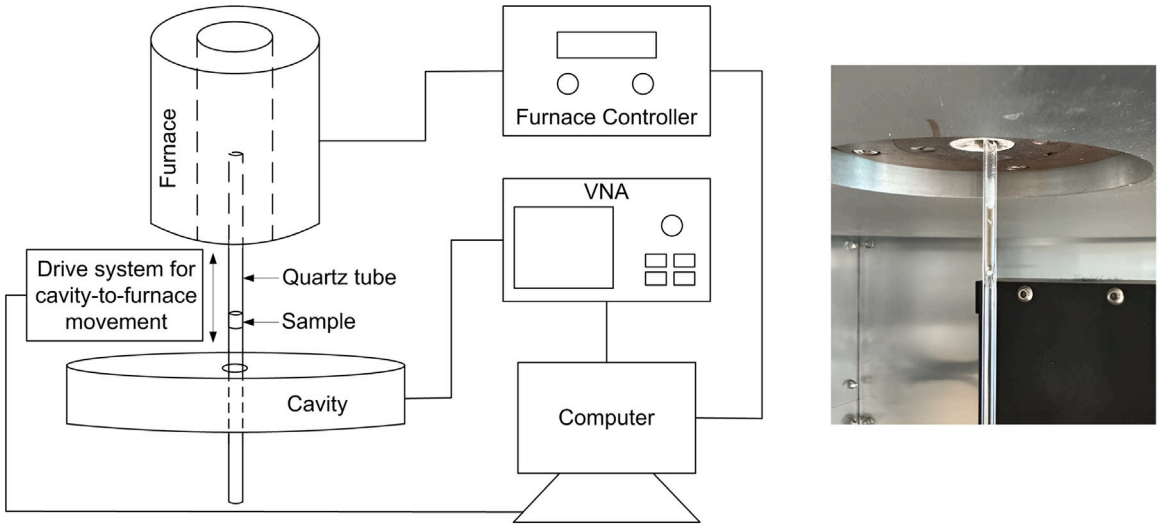

Fig. 3. Flow diagram of the TM_{020} (912 MHz) and TM_{050} (2.45 GHz) cavity system (left), and photograph of the quartz tube containing solar salt (right).

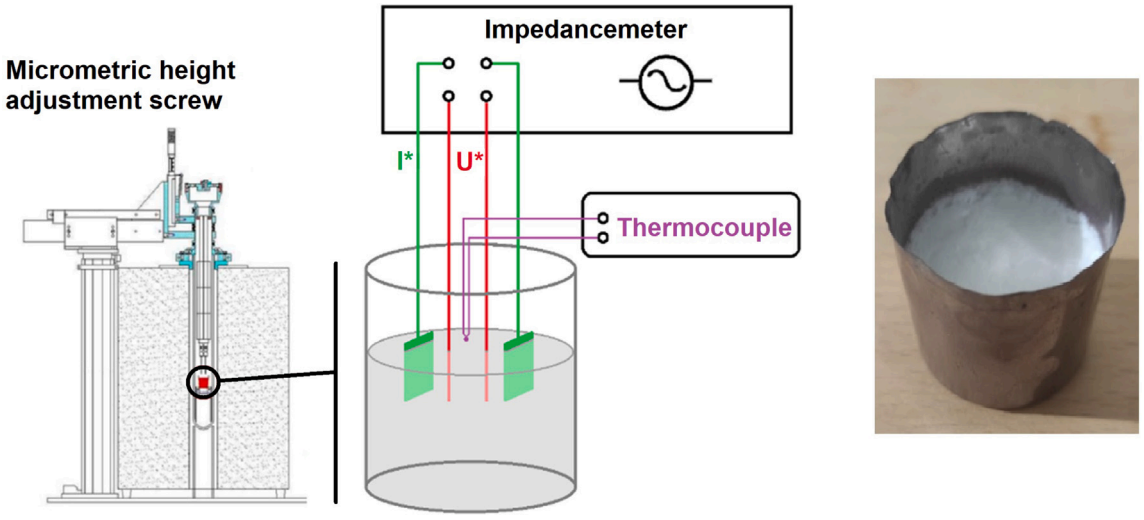

Fig. 4. Schematic of the four-electrode electrochemical impedance spectroscopy (EIS) setup [41] (left), and photograph of the gold–palladium (Au–Pd) crucible containing solar salt (right).

(iii) a final heating to 550 °C to withdraw the electrodes while the sample was in the liquid state. The heating and cooling rates were maintained constant at 2 °C min^{-1}. Measurements were conducted using a Solartron SI 1260 impedance analyser over the 100 Hz–1 MHz frequency range with an excitation voltage of 0.5 V_{rms}.

The complex impedance was expressed as $Z^* = Z' + jZ''$, where the real part $Z' = R$ represents the resistive contribution and the imaginary part $Z'' = X$ corresponds to the capacitive and inductive components of the sample. The complex conductivity $\sigma^* = \sigma' + j\sigma''$ was calculated from the impedance data using the geometric cell factor (f_{geo}) determined by calibration with a standard potassium chloride (KCl) solution of known conductivity:

$$\sigma^* = \frac{f_{geo}}{Z^*} \tag{15}$$

The dielectric components are related to the impedance through Eqs. (16)–(17), with ε''_{eff} following the conduction-loss approximation previously introduced in Eq. (3):

$$\varepsilon''_{eff} = \frac{\sigma'}{\omega\varepsilon_0} = f_{geo}\frac{-R}{2\pi f\,\varepsilon_0\,(R^2+X^2)} \tag{16}$$

$$\varepsilon' = f_{geo}\frac{-X}{2\pi f\,\varepsilon_0\,(R^2+X^2)} \tag{17}$$

where σ_{dc} corresponds to purely resistive behaviour (i.e., $X \to 0$) and is obtained from the impedance spectra as the low-frequency limit of σ', excluding electrode polarisation, or, equivalently, from the intercept with the real axis of the main semicircle in the Cole–Cole (Nyquist) diagrams at different temperatures [42], as given by Eq. (18):

$$\sigma_{dc} = \frac{f_{geo}}{R_{dc}} \tag{18}$$

This value reflects the intrinsic ionic conductivity, corresponding to the frequency-independent plateau of $\sigma'(f)$.

3. Results and discussion

3.1. Cavity perturbation measurements

This subsection summarises the results obtained using the different CPM-based experimental setups employed in this study.

3.1.1. Permittivity obtained in the dual-mode cylindrical cavity

Fig. 5 presents the evolution of ε' and ε'' as a function of temperature, obtained using the CPM method with the dual-mode cylindrical cavity described in Section 2.2.1. To ensure representativeness and

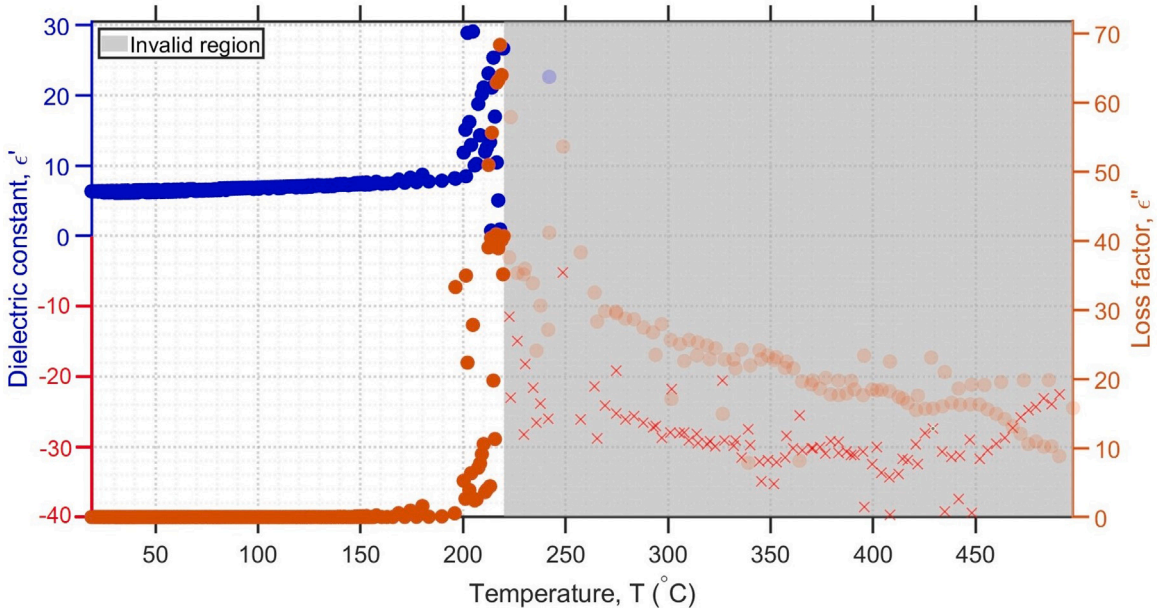

Fig. 5. Profiles of the dielectric properties (ε', ε'') of solar salt as a function of temperature measured at 2.45 GHz using the dual-mode cylindrical cavity.

repeatability, up to three heating and cooling cycles were performed on two solar salt samples of equal volume.

Up to approximately 200 °C, the dielectric properties remain nearly constant. ε' starts at 6.35 at 20 °C and gradually increases to about 8.4 around 200 °C, where an abrupt rise is observed, reaching values close to 30 within this temperature region. Beyond 220 °C, which corresponds to the melting point of solar salt, non-physical (negative) values are recorded. This behaviour is attributed to the phase transition from a solid dielectric to a highly conductive liquid, driven by the sharp increase in ionic mobility. Under these conditions, the conductivity rises markedly, modifying the electromagnetic field distribution inside the cavity and exceeding the sensitivity range of the CPM, thereby reducing the reliability of ε^* estimation.

Solar salt experiences a density change of approximately 4.6% upon melting [15]. This variation is not incorporated into the CPM analysis because its impact is negligible compared with the fundamental limitation that arises when the material becomes molten and highly conductive, at which point the small-perturbation assumption fails. Furthermore, the CPM analysis assumes a cylindrical sample with a perfectly flat upper surface. In practice, solar salt forms a slightly convex free surface due to surface-tension effects [43]. To the authors' knowledge, no dedicated studies have systematically analysed how such curvature influences CPM accuracy.

Regarding ε'', it remains practically unchanged in the solid state, with values close to 0.02. A slight increase is observed as the temperature approaches 200 °C, reaching approximately 0.5. This behaviour may be related to structural rearrangements occurring before melting or to the onset of material softening. Finally, similar to ε', ε'' exhibits an abrupt increase characteristic of a thermal-runaway phenomenon once the solar salt changes phase.

3.1.2. Permittivity and interaction with electric and magnetic fields in the rectangular cavity

Measurements with the single-mode TE_{104} cavity were performed during heating and cooling cycles between room temperature and 550 °C. To assess repeatability, up to three measurements were conducted for each experimental configuration. To mitigate the effects of the high dielectric losses of molten solar salt, two sample volumes were evaluated (heights of 10 mm and 2 mm). Although both provided consistent values in the solid state, the 10 mm sample exhibited large uncertainties after melting, with errors up to ±70 in ε'. Reducing the height to 2 mm, together with the synthetic calibration [24], significantly improved measurement accuracy.

Fig. 6 shows a clear hysteresis between the heating and cooling curves, associated with the difference between the melting and crystallisation temperatures of this non-eutectic nitrate mixture [15]. In the solid state, both volumes yield nearly identical values ($\varepsilon' \approx 5$), with a gradual increase up to ~ 220 °C. This increase is more pronounced for the 10 mm sample, which reaches $\varepsilon' \approx 8.5$ compared with $\varepsilon' \approx 6$ for the 2 mm sample, because the larger volume remains longer in a partially molten state, whereas the reduced sample undergoes a more abrupt solid–liquid transition. The heating values for the 10 mm sample are lower than those obtained during cooling, indicating a lower effective ε' associated with the porosity of the granular material when initially loaded into the quartz tube.

Between 265 and 290 °C, ε' increases more sharply and exhibits significant dispersion for both $h = 10$ mm and $h = 2$ mm. Above 290 °C, once the salt is fully molten, the 2 mm sample shows considerably lower uncertainty (±7). These results confirm that, for high-loss materials, reducing the sample volume improves the validity of the small-perturbation assumption and therefore the accuracy of the measurement. In the liquid regime, ε' stabilises around 40 and gradually increases to ~ 56 at 500 °C. The difference in maximum temperatures observed for each volume can be attributed to the faster cooling rate of the 2 mm sample, resulting from its lower thermal mass and higher surface-to-volume ratio.

Temperature was monitored using a pyrometer directed at the free surface of the molten salt, in contrast to the dual-mode cylindrical cavity, where the temperature is inferred from the quartz-tube wall. Although emissivity data for solar salt are available [44], this study assumed an emissivity of 100% and did not account for the slight convex curvature that forms on the melt surface due to surface tension [43].

Fig. 7 presents the temperature-dependent evolution of ε'' obtained directly from the reduced and calibrated sample. The trend was similar to that of ε', with a clear increase in this dielectric property once the material began to melt. In the solid state at room temperature, ε'' was approximately 0.02 and remained nearly constant, exhibiting only a slight increase up to about 220 °C, where it reached values near 0.1. Above this temperature, both ε' and ε'' showed a pronounced rise accompanied by large uncertainties. The loss factor ε'' reached a maximum of nearly 10 at around 290 °C, with associated errors on the order of ±40. Beyond this point, within the typical operating temperature

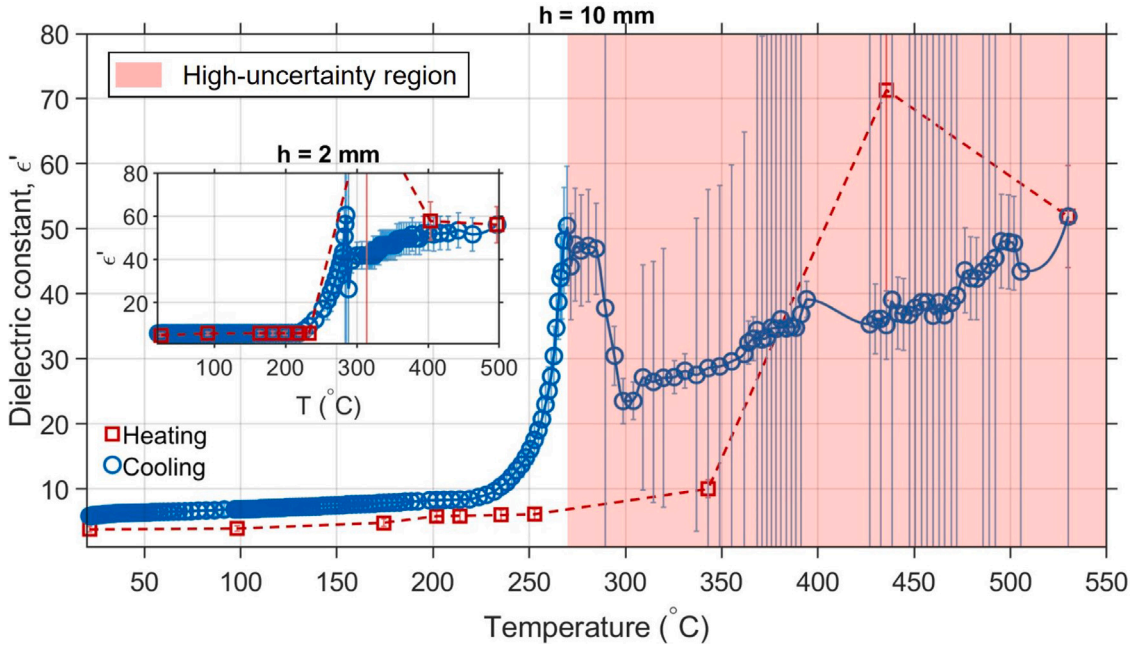

Fig. 6. Dielectric constant (ε') of solar salt for sample heights of - h = 10 mm and h = 2 mm — as a function of temperature at 2.45 GHz.

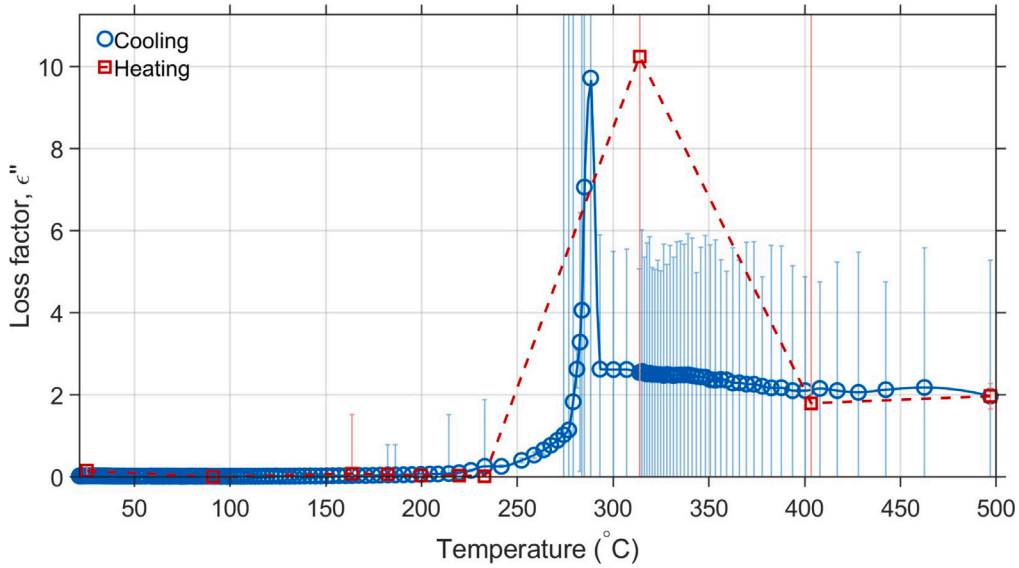

Fig. 7. Dielectric loss factor (ε'') of solar salt for a sample height of h = 2 mm as a function of temperature at 2.45 GHz.

range of the storage medium, ε'' stabilised at approximately 2.5 and gradually decreased to about 2 at 550 °C.

As described in Section 2.2.2, the short-circuited WR340 waveguide includes two apertures at the H-field maximum, allowing the sample to be positioned at either the E- or H-field antinode. Fig. 8 shows the resulting resonant frequency (f_r) and Q for the two studied volumes (10 mm and 2 mm).

Both volumes exhibited a drop in f_r during the sol id-liquid transition, consistent with the increase in ε' associated with enhanced ion mobility in the molten state. This response occurs at the E-field antinode. Under predominant H-field excitation, f_r remained essentially constant. Only a slight increase was observed for the larger volume, likely caused by weak E-field sensitivity in peripheral regions of the sample.

The Q-factor for the 10 mm sample decreased by more than one order of magnitude near melting, reflecting the strong conductive losses of molten solar salt. At higher temperatures, Q increased again; however, this "rebound" is artificial. Once D_p becomes superficial, only a thin outer layer contributes to dissipation, effectively reducing the lossy volume while intrinsic losses continue to grow.

The 2 mm sample showed the same behaviour with reduced intensity, indicating weaker field perturbation and improved measurement stability, although the Q-rebound persisted. This confirms that the small-perturbation condition was not fully met, and further volume reduction would be needed for accurate dielectric extraction. Measurements at the H-field antinode showed only a moderate decrease in Q, consistent with conduction-loss heating dominated by eddy-current generation under microwave exposure.

3.1.3. Permittivity obtained at 912 MHz and 2.45 GHz

Fig. 9 shows the temperature dependence of ε' and ε'' at 912 MHz and 2.45 GHz. As described in Section 2.2.3, the cylindrical cavity operates in the TM_{020} and TM_{050} modes, and the 4 mm quartz tube ensured

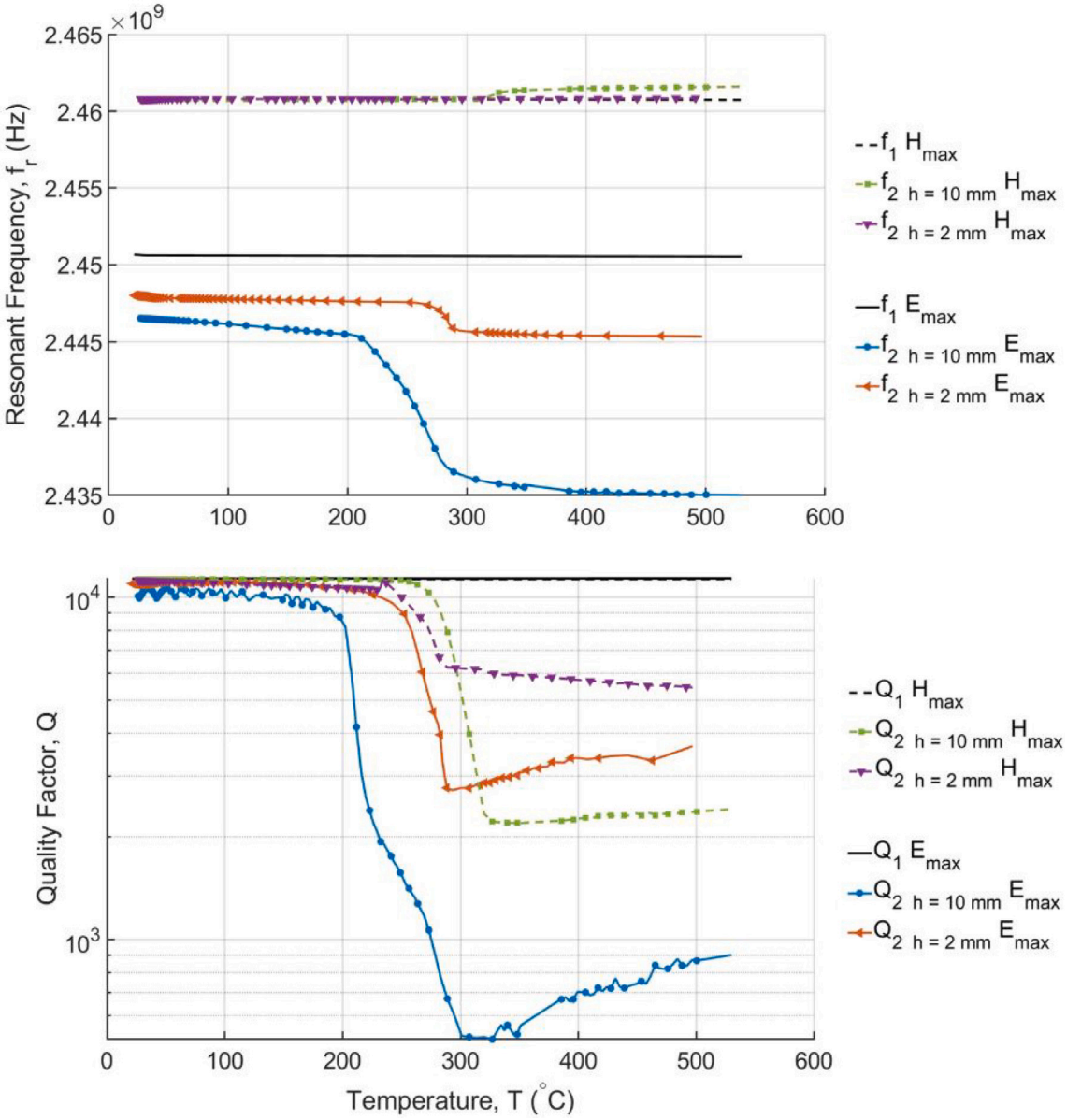

Fig. 8. Resonant frequency (f_r) and quality factor (Q) measured at the points of maximum electric (E) and magnetic (H) fields in the TE_{104} cavity, with the quartz tube either empty or filled with solar salt to heights of h = 10 mm and h = 2 mm.

stable measurements up to 300 °C. The results correspond to discrete heating steps, with the sample held at each target temperature for 10 minutes before measurement in order to ensure a uniform internal temperature; however, this procedure does not account for the thermal losses that may occur during transfer from the furnace. To verify the consistency of the results, repeated measurements were performed under the same experimental conditions, yielding reproducible trends within the experimental uncertainty.

For ε', this remained nearly constant in the solid state, with values around 3.5 up to 100 °C. A moderate increase was observed on heating to 150 °C (approximately 5.4), followed by a gradual rise to about 7 between 200 °C and 300 °C. Uncertainties within this range remained within ±0.5–1.5.

Above 300 °C, ε' increased sharply, reflecting the transition to the molten, highly conductive state. At 350 °C, values of 22.5 at 2.45 GHz and 29.8 at 912 MHz were obtained, converging to approximately 34 at 400 °C. The higher losses and enhanced ionic mobility in this regime led to markedly larger uncertainties (±9 at 350 °C and ±12 at 400 °C). At 450 °C, both frequencies yielded $\varepsilon' \approx 40$, although with uncertainties approaching ±20 owing to the high conductivity of the molten salt.

For ε'', the loss factor remained extremely low in the solid state (around 0.002 with uncertainties of ±0.001) and increased slowly to approximately 0.06 at 300 °C. Upon melting, ε'' rose abruptly, reaching values of around 4 at 350 °C and approximately 11 at 450 °C. As with ε', uncertainties increased substantially in the molten state (up to ±9), reflecting the intrinsic limitations of the CPM under these conditions.

Fig. 9 also compares these results with those from the dual-mode cavity and the TE_{104} cavity (cooling only), which are plotted with thinner lines for clarity. A clear hysteresis between heating (TM020 at 912 MHz and TM050 at 2.45 GHz) and cooling (TE_{104}) is observed, consistent with the non-eutectic behaviour of the nitrate mixture [15]. In the solid state, the ε' values measured with the TM_{0n0} cavity tend to be slightly lower, which is likely related to the granular and partially porous nature of the packed powder, effectively reducing the apparent ε'.

Once molten, the discrepancies observed between cavities in both ε' and ε'' mainly reflect the intrinsic difficulty of characterising a

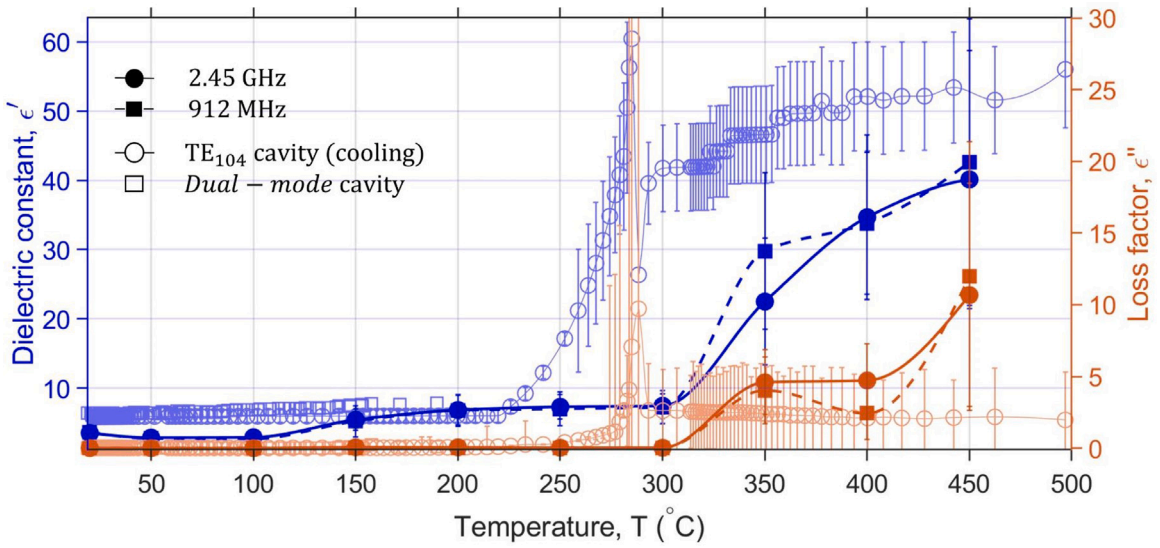

Fig. 9. Dielectric properties (ε', ε'') of solar salt as a function of temperature measured at 2.45 GHz and 912 MHz, including comparison with TE_{104} and dual-mode cavity measurements at 2.45 GHz.

highly conductive liquid using resonant techniques, for which reliable measurements require very small sample volumes and the perturbation assumption approaches the limits of its validity. Additional systematic differences arise from the temperature determination methods, as in the TE_{104} cavity the temperature is measured by pyrometry at the molten salt surface assuming unit emissivity, whereas in the dual-mode cavity it is inferred from the quartz-tube wall. For the cylindrical cavity operating at 912 MHz and 2.45 GHz, measurements were performed after discrete heating steps with a 10 min dwell time; however, this procedure does not fully account for heat losses during sample transfer. These factors, together with the ~4.6% density change upon melting and the slightly convex free surface induced by surface-tension effects, provide a consistent explanation for the systematic offsets observed between devices without affecting the overall trends or conclusions.

3.2. Electrochemical impedance measurements

The measurements obtained by EIS provide comprehensive information on the ionic mobility of the analysed material. The tests were performed over a frequency range from 100 Hz to 1 MHz, recording results at different temperatures, from the solid state (approximately 150 °C) up to the liquid phase, with a maximum limit of 524 °C.

3.2.1. Frequency dependence

At a given temperature, σ of predominantly ionic materials shows a clear frequency dependence [45]. Fig. 10 shows the variation of σ' as a function of frequency for different temperatures. In all cases, a nearly constant region – or plateau – can be observed in the intermediate frequency range, corresponding to σ_{dc} associated with long-range ionic transport. As expected, σ_{dc} progressively increases with temperature.

At low frequencies, σ' decreases due to the electrode polarisation (EP) phenomenon, which originates from the accumulation of charge carriers at the electrode-sample interface. This effect is extrinsic to the material and is characteristic of ionic conductors with blocking electrodes. The contribution of EP becomes more pronounced at high temperatures and low frequencies, where ionic mobility promotes charge accumulation on the electrode surfaces [46].

In the intermediate frequency range, a domain of constant ionic conductivity can be identified, while at higher frequencies a dispersive region appears, characterised by an increase in σ' with frequency. This behaviour is associated with the localised motion of ions within potential wells or between neighbouring sites of the network. At elevated temperatures, the mobility of charge carriers becomes so high that the dispersive region shifts beyond the measurement range of the equipment (approximately 1 MHz), and therefore almost disappears from the curves.

The impedance spectra were corrected to eliminate the inductive contribution of the measurement cables and electrical connections. Fig. 11 illustrates this correction for the Nyquist plot obtained at 200 °C. This Z'' correction becomes increasingly relevant at temperatures above 200 °C, as the total impedance of the molten salt decreases and the relative influence of parasitic inductance becomes more pronounced. After correction, the high-frequency end of the curve aligns with the real axis, yielding a smoother semicircle and allowing an accurate determination of the bulk resistance (R_{dc}). The corresponding σ_{dc} is then calculated according to Eq. (18).

Fig. 12 presents the evolution of the corrected Nyquist diagrams ($-X$ vs. R) obtained at different temperatures during the cooling cycle of solar salt. The impedance response exhibits the typical response of an ionic conductor, characterised by a semicircular arc at intermediate frequencies followed by a low-frequency tail associated with EP.

At low temperatures (150–200 °C), the impedance modulus is high and the Nyquist plots display well-defined semicircles, indicating dominant capacitive behaviour and limited ionic mobility. As temperature increases, the radius of the semicircle progressively decreases, reflecting the thermally activated nature of ionic transport. Above approximately 250 °C, the arcs become increasingly flattened, and at higher temperatures (≥ 350 °C) the curves evolve towards nearly vertical lines, suggesting a transition to a purely conductive response dominated by ion motion in the molten state.

3.2.2. Temperature dependence

Fig. 13 shows σ' of solar salt as a function of temperature for different frequencies during the heating and cooling processes. Similar to the measurements performed by CPM at ISM microwave frequencies, solar salt exhibits a marked change in conductivity when reaching the phase-transition temperatures — crystallisation and melting. As the temperature increases, the ionic mobility rises, resulting in a progressive increase in σ'.

In the liquid state, the curves corresponding to 100 Hz and 1 kHz display similar values, around 100–110 S/m at 524 °C. The 10 kHz curve shows higher σ' throughout the 224–524 °C range (up to approximately 130 S/m), while at 100 kHz σ' continues to increase, reaching about 160 S/m. However, at 1 MHz the rate of increase of conductivity with temperature decreases, giving a final value of

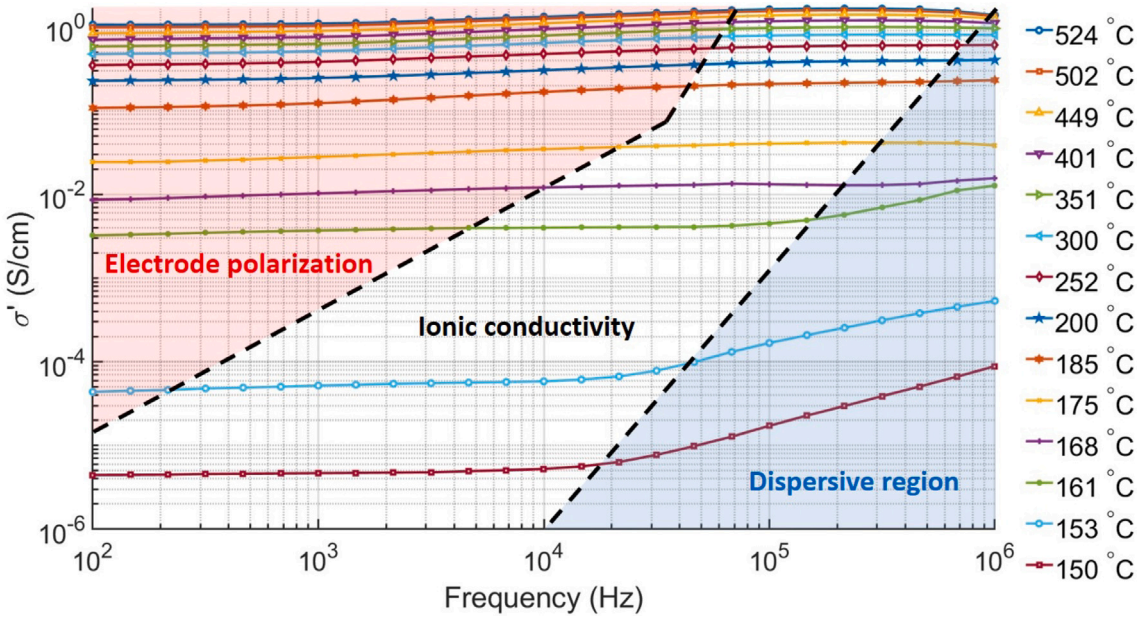

Fig. 10. Frequency dependence of the real part of the electrical conductivity (σ') of solar salt at different temperatures.

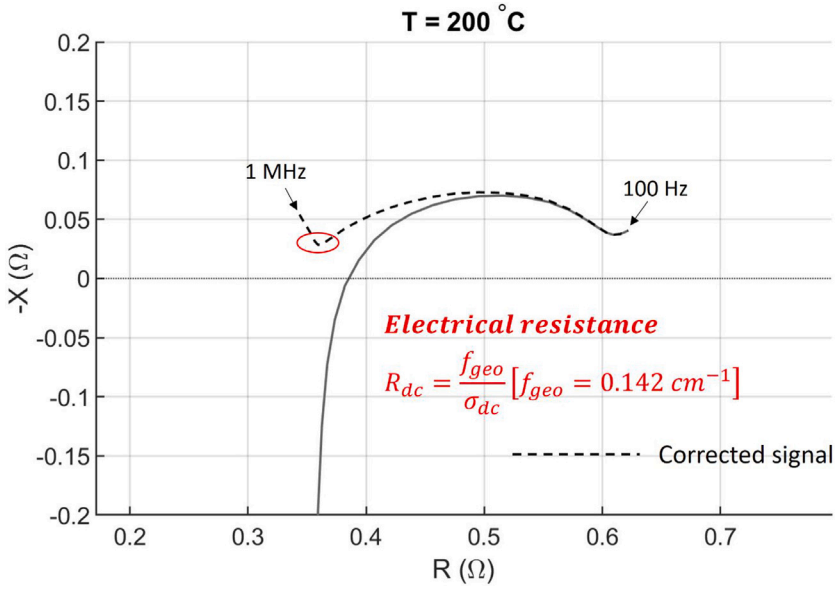

Fig. 11. Correction of the inductive contribution in the imaginary part of the impedance (Z'') at 200 °C.

130 S/m at 524 °C. This behaviour can be attributed to a combination of dipolar dispersion phenomena and the inductive contribution of the measurement system at high frequencies, which together reduce the apparent ionic conductivity observed above several hundred kilohertz.

To identify the different states of solar salt during the heating process, the Arrhenius plot of σ_{dc} was constructed (Fig. 14). In each temperature region, the activation energy (E_a) was obtained from the slope of the linear regression according to the Arrhenius law, expressed as:

$$\ln \sigma_{dc} = -\frac{E_a}{k_B}\left(\frac{1}{T}\right) + \ln A \tag{19}$$

where T is the temperature in kelvin, A is the pre-exponential factor, E_a is the activation energy, and k_B is the Boltzmann constant (8.617×10^{-5} eV K^{-1}).

In the liquid state, the curve exhibits an almost flat slope (E_a = 0.148 eV), indicative of high ionic mobility governed by the free motion of mobile ions, leading to high conductivity and weak temperature dependence. Around 220–224 °C, an abrupt slope change is observed, marking the onset of solidification and a pronounced drop in ionic mobility, coinciding with the melting temperature of solar salt. Between 217 and 180 °C, in this transition interval, the electrical behaviour corresponds to a partially crystallised liquid. Finally, the slope decreases slightly (E_a = 0.810 eV), corresponding to a fully crystalline solid where ionic mobility is minimal and the electrical response is practically insulating.

3.2.3. Approximation to microwave frequencies

The frequency range covered by EIS (100 Hz–1 MHz) does not overlap with the microwave domain probed by the CPM measurements (912 MHz and 2.45 GHz). Nevertheless, an approximate estimation of the microwave conductivity can be inferred from the frequency evolution of σ' in the molten state, following Jonscher's universal dielectric

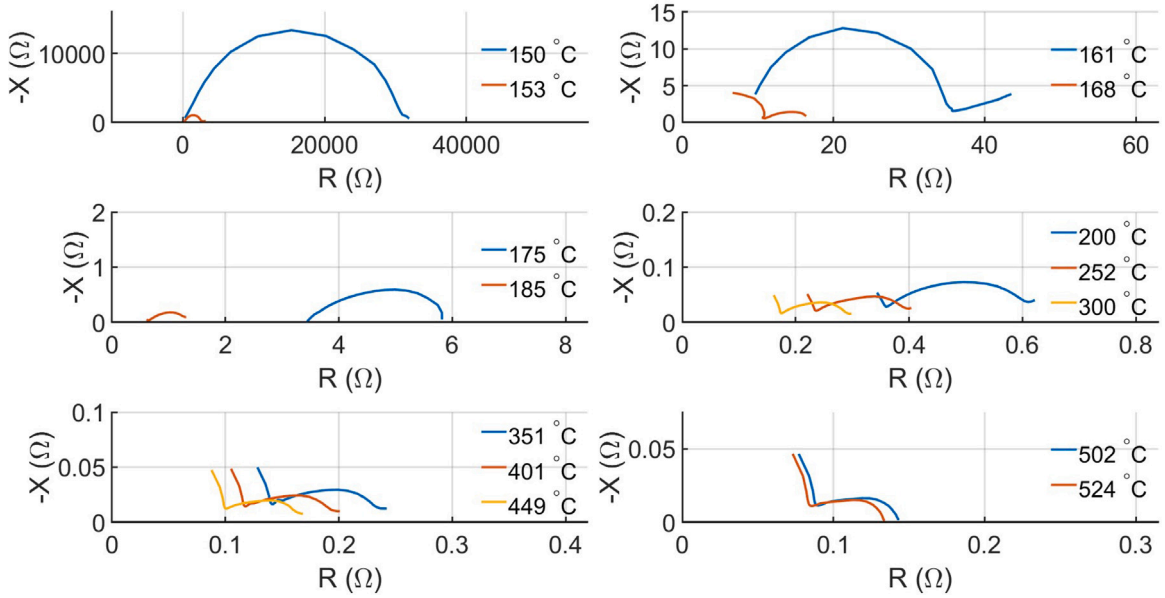

Fig. 12. Nyquist plots of the complex impedance (Z^*) for solar salt at selected temperatures.

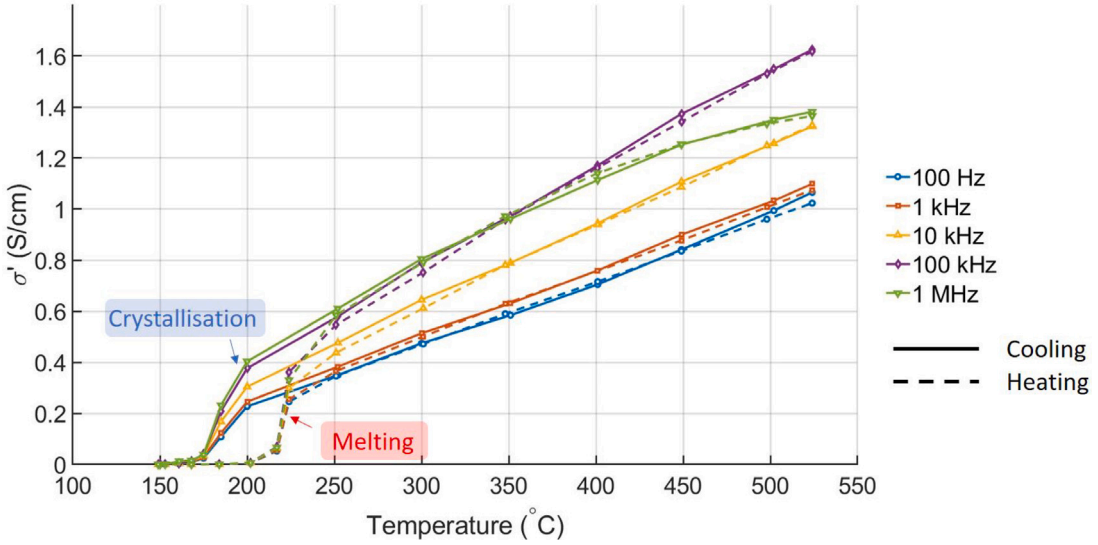

Fig. 13. Real part of the electrical conductivity (σ') as a function of frequency for solar salt at different temperatures.

response (UDR) model [45]. Within this model, $\sigma'(\omega) = \sigma_{dc} + A\omega^s$, where $0 < s < 1$ characterises the dispersive regime associated with localised ion dynamics.

At 524 °C, the EIS spectra (Fig. 10) show a well-defined plateau characteristic of σ_{dc}, with σ'(100 Hz) ≈ 107 S/m and σ'(1 MHz) ≈ 138 S/m, representing an increase of less than 30% over four decades. A log–log fit of the high-frequency segment (10 kHz–1 MHz) yields a dispersion exponent of $s \simeq 0.02$, confirming the extremely weak frequency dependence of solar salt in the liquid phase within this frequency range.

Assuming that this trend extends into the microwave region, values were extrapolated from 1 MHz using $\sigma'(f) \propto f^s$. For $s = 0.02$, this yields σ'(912 MHz) ≈ 160 S/m and σ'(2.45 GHz) ≈ 160–170 S/m. Using these values in the expressions for ε' and ε'' (Eqs. (16) and (17)), $\tan\delta = \varepsilon''/\varepsilon'$ was calculated and substituted into Eq. (4), yielding Dp of approximately 1.3 mm at 912 MHz and 0.8 mm at 2.45 GHz. These values fall within the conduction-dominated regime ($\tan\delta \gg 1$), where the D_p approaches the classical skin-depth behaviour and becomes mainly governed by σ' [47]. The main uncertainty in these estimates arises from extrapolating σ' into the GHz range; thus, the resulting D_p values should be regarded as approximations, although they remain consistent with the trends observed in the CPM measurements.

4. Conclusions and outlook

In this study, the dielectric behaviour of solar salt was characterised using complementary CPM and EIS. The CPM measurements were performed at 912 MHz and 2.45 GHz, corresponding to ISM frequency bands, while EIS measurements were performed over the frequency range from 100 Hz to 1 MHz. The use of EIS was essential to complement CPM, which becomes unreliable in the molten phase due to the breakdown of the small-perturbation assumption under highly lossy conditions. Together, the two techniques consistently showed that solar salt undergoes a transition from a dielectric solid to a highly conductive liquid, in which charge dynamics are dominated by ionic motion.

In the solid state, solar salt behaves as a low-loss dielectric, with ε' values of approximately 5–7 and ε'' around 0.02. As the material

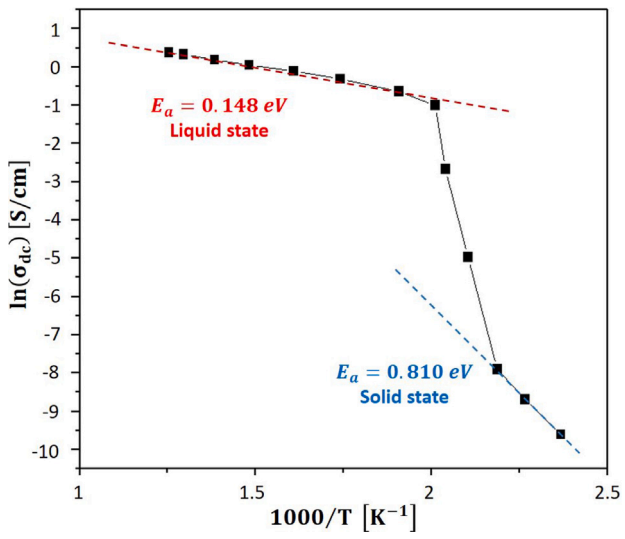

Fig. 14. Arrhenius plot of the direct conductivity (σ_{dc}) of solar salt.

approaches and undergoes melting, both dielectric parameters increase sharply, reflecting the onset of ionic conduction. Across all CPM configurations, reliable determination of ε^* was only possible up to the solid–liquid phase transition. In the dual-mode cylindrical cavity, the combination of simultaneous heating and measurement enabled stable measurements up to approximately 220 °C; beyond this temperature, ε' became negative and physically unreliable, marking the breakdown of the small-perturbation assumption in the molten phase. Similar limitations were observed in the rectangular TE_{104} cavity, even when the effective calibration height was reduced to 2 mm using quartz tubes with an 8 mm inner diameter, as well as in the cylindrical cavity operated in the TM_{020} and TM_{050} modes at 912 MHz and 2.45 GHz with a 4 mm internal diameter. Although reducing the effective sample height improved measurement stability in the TE_{104} configuration, the rebound observed in Q indicated that the perturbation condition was still not fully satisfied, suggesting that even smaller effective sample volumes would be required for accurate dielectric characterisation of molten solar salt. Measurements performed at the H-field antinode showed only a moderate decrease in Q, consistent with conduction-loss heating dominated by eddy currents.

The EIS measurements confirmed the trends observed with CPM, revealing a clear transition from capacitive to conductive behaviour across the solid–liquid phase change, accompanied by a strong decrease in R_{dc}. Arrhenius analysis of σ_{dc} identified two distinct conduction regimes, with $E_a = 0.810$ eV in the solid state and $E_a = 0.148$ eV in the liquid state. Extrapolation of the EIS data to the GHz frequency range yielded $\sigma' \approx 160$–170 S/m. From these values, D_p of ≈1.3 mm at 912 MHz and ≈0.8 mm at 2.45 GHz were estimated. Although approximate, these results are consistent with the CPM observations and indicate that microwave absorption in molten solar salt is largely confined to near-surface regions.

These findings have direct implications for the optimisation of PtHtP systems employing solar salt as a TES medium. The shallow D_p observed in the molten phase suggests that purely volumetric microwave heating is difficult to achieve. Consequently, future system designs may benefit from hybrid configurations in which microwave-transparent ceramic structures, already widely used in TES technologies, are incorporated to increase the effective D_p and promote more uniform heat distribution. In line with CB operating principles, one promising approach involves heating liquid solar salt as it flows from the cold tank to the hot tank through a microwave-transparent tube containing a ceramic honeycomb or open-foam structure housed within a microwave cavity. Further work along this research line will therefore require dedicated studies of the dielectric properties of suitable ceramic materials, as well as investigations into the influence of their geometry, porosity and interaction with flowing solar salt on heating uniformity, achievable temperature levels and thermal control.

From an experimental standpoint, the limited D_p of molten solar salt highlights the need for CPM systems adapted to highly conductive materials. In this context, *in situ*-heating and measurement enable dielectric characterisation without thermal losses associated with sample transport, ensuring reliable temperature data.

CRediT authorship contribution statement

C. Valverde: Writing – review & editing, Writing – original draft, Visualization, Validation, Methodology, Investigation, Formal analysis, Data curation, Conceptualization. **G. Link:** Writing – review & editing, Validation, Supervision, Resources, Methodology. **S. Soldatov:** Writing – review & editing, Validation, Supervision, Resources, Methodology. **J.M. Catalá-Civera:** Supervision, Resources. **P. Plaza-González:** Supervision, Resources. **G. Dimitrakis:** Writing – review & editing, Validation, Investigation, Formal analysis. **B. Singh:** Writing – review & editing, Validation, Investigation, Formal analysis. **A. Cachot:** Writing – review & editing, Validation, Investigation, Formal analysis. **L. Del Campo:** Writing – review & editing, Validation, Investigation, Formal analysis. **M. Malki:** Writing – review & editing, Validation, Investigation, Formal analysis. **M.M. Rodriguez-Garcia:** Supervision, Funding acquisition. **E. Rojas:** Supervision.

Declaration of competing interest

The authors declare that they have no known competing financial interests or personal relationships that could have appeared to influence the work reported in this paper.

Acknowledgements

This work was supported by the European Energy Research Alliance (EERA) through the EERA Joint Programme on Energy Storage – Mobility Scheme for Young Researchers (2025). This financial support enabled a three-month research stay at the Karlsruhe Institute of Technology (KIT).

This research was also carried out within the framework of the GREENOLIVE project (Project ID: *GREENOLIVE A_T_2.1_0213*), funded under the Interreg NEXT MED Programme co-funded by the European Union.

Data availability

Data will be made available on request.

References

[1] de Sisternes FJ, Jenkins JD, Botterud A. The value of energy storage in decarbonizing the electricity sector. Appl Energy 2016;175:368–79. http://dx.doi.org/10.1016/j.apenergy.2016.05.014.

[2] The Royal Society. Low-carbon heating and cooling: overcoming one of world's most important net zero challenges. Tech. rep., Royal Society; 2021, URL https://policycommons.net/artifacts/1628411/low-carbon-heating-and-cooling/.

[3] Bouckaert S, Pales AF, McGlade C, Remme U, Wanner B, Varro L, D'Ambrosio D, Spencer T. Net zero by 2050: A roadmap for the global energy sector. 2021.

[4] Obi M, Bass R. Trends and challenges of grid-connected photovoltaic systems – A review. Renew Sustain Energy Rev 2016;58:1082–94. http://dx.doi.org/10.1016/j.rser.2015.12.289.

[5] Grolms M. Power-To-Heat-To-Power. Advanced Science News; 2019, URL https://www.advancedsciencenews.com/power-to-heat-to-power/.

[6] Okazaki T. Electric thermal energy storage and advantage of rotating heater having synchronous inertia. Renew Energy 2020;151:563–74. http://dx.doi.org/10.1016/j.renene.2019.11.051.

[7] Boroojeni KG, Amini MH, Nejadpak A, Iyengar S, Hoseinzadeh B, Bak CL. A theoretical bilevel control scheme for power networks with large-scale penetration of distributed renewable resources. In: 2016 IEEE international conference on electro information technology. EIT, 2016, p. 0510–5. http://dx.doi.org/10.1109/EIT.2016.7535293.

[8] Zurita A, Mata-Torres C, Valenzuela C, Felbol C, Cardemil JM, Guzmán AM, Escobar RA. Techno-economic evaluation of a hybrid CSP + PV plant integrated with thermal energy storage and a large-scale battery energy storage system for base generation. Sol Energy 2018;173:1262–77. http://dx.doi.org/10.1016/j.solener.2018.08.061.

[9] Achkari O, El Fadar A. Latest developments on TES and CSP technologies - energy and environmental issues, applications and research trends. Appl Therm Eng 2020;167. http://dx.doi.org/10.1016/j.applthermaleng.2019.114806.

[10] Novotny V, Basta V, Smola P, Spale J. Review of carnot battery technology commercial development. Energies 2022;15(2):647. http://dx.doi.org/10.3390/en15020647.

[11] Han Y, Sun Y, Wu J. A low-cost and efficient solar/coal hybrid power generation mode: Integration of non-concentrating solar energy and air preheating process. Energy 2021;235:121367. http://dx.doi.org/10.1016/j.energy.2021.121367.

[12] Crespo L. The double role of CSP plants on the future Electrical Systems. Bloomberg NEF; 2020, URL https://about.bnef.com/blog/battery-pack-prices-cited-below-100-kwh-for-the-first-time-in-2020-while-market-average-sits-at-137-kwh/.

[13] Alva G, Liu LK, Huang X, Fang GY. Thermal energy storage materials and systems for solar energy applications. Renew Sustain Energy Rev 2017;68:693–706. http://dx.doi.org/10.1016/j.rser.2016.10.021.

[14] Bauer T, Odenthal C, Bonk A. Molten salt storage for power generation. Chem Ing Tech 2021;93(4):534–46. http://dx.doi.org/10.1002/cite.202000137.

[15] Rodríguez-García M-M, Herrador-Moreno M, Zarza Moya E. Lessons learnt during the design, construction and start-up phase of a molten salt testing facility. Appl Therm Eng 2014;62(2):520–8. http://dx.doi.org/10.1016/j.applthermaleng.2013.09.040.

[16] Cordaro JG. Chemical perspectives on alkali and earth alkaline nitrate and nitrite salts for concentrated solar power applications. Green 2013;3(1):9–18. http://dx.doi.org/10.1515/green-2012-0026.

[17] Martin A, Navarrete A. Microwave-assisted process intensification techniques. Curr Opin Green Sustain Chem 2018;11:70–5. http://dx.doi.org/10.1016/j.cogsc.2018.04.019.

[18] Binnen JGP, Cross TE, Greenacre NR, Naser-Moghadasi M. High temperature dielectric property measurements — An insight into microwave loss mechanisms in engineering ceramics. MRS Online Proc Libr 1994;347(1):247–52. http://dx.doi.org/10.1557/PROC-347-247.

[19] Catala-Civera JM, Canos AJ, Plaza-Gonzalez P, Gutierrez JD, Garcia-Banos B, Penaranda-Foix FL. Dynamic measurement of dielectric properties of materials at high temperature during microwave heating in a dual mode cylindrical cavity. IEEE Trans Microw Theory Tech 2015;63(9):2905–14. http://dx.doi.org/10.1109/tmtt.2015.2453263.

[20] Chen LF, Ong CK, Neo CP, Varadan VV, Varadan VK. Microwave electronics: Measurement and materials characterization. Hoboken, NJ: Wiley & Sons; 2004.

[21] Bethe HA, Schwinger J. Perturbation theory for cavities. Tech. rep., Cornell University; 1943.

[22] Rueggeberg W. Determination of complex permittivity of arbitrarily dimensioned dielectric modules at microwave frequencies. IEEE Trans Microw Theory Tech 1971;19(6):517–21. http://dx.doi.org/10.1109/TMTT.1971.1127567.

[23] Nesbitt A, Navabpour P, Degamber B, Nightingale C, Mann T, Fernando G, Day RJ. Development of a microwave calorimeter for simultaneous thermal analysis, infrared spectroscopy and dielectric measurements. Meas Sci Technol 2004;15(11):2313–24. http://dx.doi.org/10.1088/0957-0233/15/11/018.

[24] Soldatov S, Kayser T, Link G, Seitz T, Layer S, Jelonnek J. Microwave cavity perturbation technique for high-temperature dielectric measurements. In: 2013 IEEE MTT-S international microwave symposium digest. MTT, 2013, p. 1–4. http://dx.doi.org/10.1109/MWSYM.2013.6697793.

[25] Lin M, Afsar MN. A new cavity perturbation technique for accurate measurement of dielectric parameters. In: 2006 IEEE MTT-S international microwave symposium digest. 2006, p. 1630–3. http://dx.doi.org/10.1109/MWSYM.2006.249650.

[26] Ma J, Wu Z, Xia Q, Wang S, Tang J, Wang K, Guo L, Jiang H, Zeng B, Gong Y. Complex permittivity measurement of high-loss biological material with improved cavity perturbation method in the range of 26.5–40 GHz. Electronics 2020;9(8):1200. http://dx.doi.org/10.3390/electronics9081200.

[27] Hachem C, Faget L, Véron E, Bessada C, Del Campo L, Cachot A, Cosson L, Sarou-Kanian V, Deschamps M. Novel approach to probe ionic species mobility in molten salts electrolyte for thermal batteries. J Power Sources 2025;652:237558. http://dx.doi.org/10.1016/j.jpowsour.2025.237558.

[28] Cornelison SG, Gauss J, Krane J, Hardy JR. Centimeter-wave reflection in the nitrates and nitrites of sodium and potassium: Experiment and theory. J Appl Phys 1997;81(3):1451. http://dx.doi.org/10.1063/1.364182.

[29] Binnen JGP, Cross TE, Greenacre NR, Naser-Moghadasi M. High temperature dielectric property measurements — An insight into microwave loss mechanisms in engineering ceramics. MRS Online Proc Libr 1994;347(1):247–52. http://dx.doi.org/10.1557/PROC-347-247.

[30] Sparks M, Loudon R, Kittel C. Ferromagnetic relaxation. I. Theory of the relaxation of the uniform precession and the degenerate spectrum in insulators at low temperatures. Phys Rev 1961;122(3):791–803. http://dx.doi.org/10.1103/PhysRev.122.791, PR.

[31] Metaxas AC, Meredith RJ. Industrial microwave heating. In: IET power engineering series, London: Peter Peregrinus Ltd.; 1983, http://dx.doi.org/10.1049/PBPO004E.

[32] Gabriel C, Gabriel S, H. Grant E, S. J. Halstead B, Michael P. Mingos D. Dielectric parameters relevant to microwave dielectric heating. Chem Soc Rev 1998;27(3):213–24. http://dx.doi.org/10.1039/A827213Z.

[33] Bhattacharya M, Basak T. A review on the susceptor assisted microwave processing of materials. Energy 2016;97:306–38. http://dx.doi.org/10.1016/j.energy.2015.11.034.

[34] van der Zaag PJ, Valk P, Rekveldt M. A domain size effect in the magnetic hysteresis of NiZn-Ferrites. Appl Phys Lett 1996;69:2927–9. http://dx.doi.org/10.1063/1.117326.

[35] Aguiar PM, Jacquinot J-F, Sakellariou D. Experimental and numerical examination of eddy (Foucault) currents in rotating micro-coils: Generation of heat and its impact on sample temperature. J Magn Reson 2009;200(1):6–14. http://dx.doi.org/10.1016/j.jmr.2009.05.010.

[36] Pérez-Campos R, Fayos-Fernández J, Monzó-Cabrera J, Martín Salamanca F, López Valentín J, Catalá-Civera JM, Plaza-González P, Sánchez-Marín JR. Dynamic permittivity measurement of Ground-Tire Rubber (GTR) during microwave-assisted devulcanization. Polymers 2022;14(17):3543. http://dx.doi.org/10.3390/polym14173543.

[37] Dakermandji G. A new method for measuring the complex permittivity of highly conducting dielectric materials at microwave frequencies [Ph.D. thesis], 1976.

[38] Altschuler HM. Handbook of microwave measurements, vol. 2, New York, NY, USA: Polytechnic Institute of Brooklyn Press; 1963.

[39] Altarawneh S, Al-Harahsheh M, Buttress A, Dodds C, Rodriguez J, Kingman S. Microwave selective heating of electric arc furnace dust constituents toward sustainable recycling: Contribution of electric and magnetic fields. J Ind Eng Chem 2021;104:521–8. http://dx.doi.org/10.1016/j.jiec.2021.09.001.

[40] Zhadan A, Sarou-Kanian V, Del Campo L, Cosson L, Malki M, Bessada C. Speciation and transport properties in molten alkali carbonates at high temperature. J Phys Chem C 2022;126(40):17234–42. http://dx.doi.org/10.1021/acs.jpcc.2c03048.

[41] Cachot A, del Campo L, Cosson L, Ory S, Veron E, Malki M. Highlighting amorphous phase separation process on cooling borosilicate melts using impedance spectroscopy. J Non-Cryst Solids 2024;641:123155. http://dx.doi.org/10.1016/j.jnoncrysol.2024.123155.

[42] Macdonald JR, Barsoukov E. Impedance spectroscopy: Theory, experiment, and applications. 2nd ed. Hoboken, NJ: John Wiley & Sons; 2005.

[43] Grosu Y, González-Fernández L, Nithiyanantham U, Faik A. Wettability control for correct thermophysical properties determination of molten salts and their nanofluids. Energies 2019;12(19):3765.

[44] Xie M, Zhu Y, Liu Y, Yuan Y, Heping T. Measurement of spectral radiative characteristics of molten salt at high temperature using emission method. Appl Therm Eng 2019;149:151–64. http://dx.doi.org/10.1016/j.applthermaleng.2018.12.046.

[45] Jonscher AK. Dielectric relaxation in solids. J Phys D: Appl Phys 1999;32(14):R57–70. http://dx.doi.org/10.1088/0022-3727/32/14/201.

[46] Ishai PB, Talary MS, Caduff A, Levy E, Feldman Y. Electrode polarization in dielectric measurements: a review. Meas Sci Technol 2013;24(10):102001. http://dx.doi.org/10.1088/0957-0233/24/10/102001.

[47] Pozar DM. Microwave engineering. 4th ed. Hoboken, NJ: Wiley; 2012.